ACS OMEGA

http://pubs.acs.org/journal/acsodf

Article

# Ternary Phase-Field Simulations of the Skin-Sublayer Structures in Poly(vinylidene fluoride) Microporous Membranes Prepared by a Nonsolvent-Induced Phase Separation

Ping Fang, Chaoyu Yang,* Ruihua Shao, Lihui Zhou, and Kang Liu

Cite This: *ACS Omega* 2021, 6, 7444−7453

Read Online

ACCESS | Metrics & More | Article Recommendations

**ABSTRACT:** In this paper, the existing phase-field model based on the nonsolvent-induced phase separation (NIPS) method was optimized. Two-dimensional simulations using the relevant parameters of a poly(vinylidene fluoride) (PVDF) membrane system were carried out, simulating and analyzing the effects of changes in initial concentrations, concentration fluctuations, and diffusion rates of the solvent on the skin layer and sublayer structures of the membranes. These simulations modeled the process of preparing PVDF microporous membranes by the NIPS method to better understand the structural development of PVDF microporous membranes under different conditions. It was found that dense skin layers were formed at the mass-transfer exchange interface of the PVDF microporous membranes, whose number increased with the decrease of the concentration fluctuation, which has little effect on the structure of the sublayer. The initial concentration of PVDF and the diffusion rate of the solvent had a little impact on the number of skin layers yet played a relatively large role in the formation time of the skin layers and the structure of the sublayers. Also, the validity of the model was verified by corresponding experiments. Hence, the model can be applied to other PVDF ternary membrane systems by modifying specific thermodynamic and kinetic parameters.

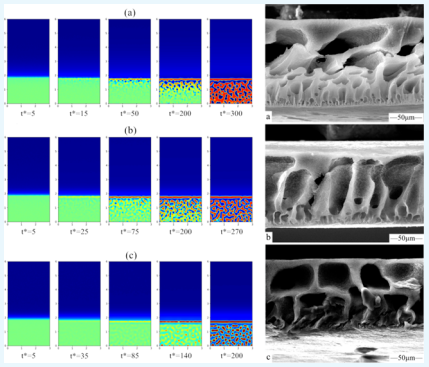

## 1. INTRODUCTION

The nonsolvent-induced phase separation (NIPS) method, also known as the immersion precipitation phase-inversion method, is the most widely used preparation method for poly(vinylidene fluoride) (PVDF) microporous membranes. The method has a simple membrane preparation process, by which the structure and performance of the membrane are adjustable, and the morphology of the prepared membrane can be continuously transformed from dense, nonporous, and sponge-like to large, finger-like pores by simply changing the initial conditions.[1−5] The membranes can be divided into symmetrical and asymmetrical types according to their structures. In practical applications, asymmetric membranes are more widely used than symmetric membranes. During the formation of an asymmetric membrane, a skin layer is first formed at the interface of the mass-transfer exchange, leading to increases in resistance to subsequent mass transfer. Such an effect is related to the compactness and thickness of the skin layer. There are several typical structures: (1) dense skin layer, whose sublayers have a sponge-like pore structure with a uniform structure; (2) dense skin layer, in which the sponge-like pore structure of the sublayers gradually increases from top to bottom; (3) dense skin layer, in which the sublayers are both finger-shaped macropores and sponge-shaped pores, and some finger-shaped macropores that are developed near the bottom of the membrane;[6] and (4) relatively dense skin layer, which is a porous skin layer where the structure of the sublayers is the same as the previous three. For these asymmetrical films, the skin layer is generally used as a selective skin layer with a thickness of 0.1−1 $\mu$m, which mainly plays a role in retention. The sublayer structure plays a supporting role and requires a certain degree of mechanical strength while maintaining a high membrane flux. Some scholars have proposed a two-step membrane formation mechanism due to this feature of the membrane structure, that is, different membrane formation mechanisms of the skin layers and the sublayers. The dense skin layers were formed from a gel, while the porous skin layers were caused by a liquid−liquid phase separation.[7−10] However, both of the formation mechanisms were complicated, including various thermodynamic and kinetic processes, such as intermolecular forces, heat- and mass-transfer processes, phase separations, crystallization, and gelation at different times and length scales, which are difficult to observe in situ and characterize through experimental means.

**Received:** December 9, 2020
**Accepted:** February 18, 2021
**Published:** March 11, 2021

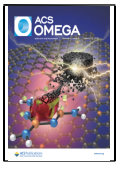





https://dx.doi.org/10.1021/acsomega.0c05982
*ACS Omega* 2021, 6, 7444−7453

The phase-field model is ideal for simulating the evolution of multiphase, large-scale, and complex microstructures, which introduces field variables (usually the partial volume fraction of the components) and uses its continuous changes to describe the local compositions at different positions in the phase region and the composition mutations at the two-phase interfaces. This determined that the phase-field theory is a powerful tool for studying the phase separation of polymer melts and solutions. The earliest research on phase-field methods can be traced back to one-dimensional simulation work on membrane-forming ternary systems of cellulose acetate/acetone/water and polyether inkstone/dimethyl acetone/water conducted by Tsay and McHugh in 1990, which investigated the influence of a nonsolvent and polymer content on the growth rate of the phase region.[11] Similar work was also carried out by Saxena and Caneba on the poly(methacrylic acid)/methacrylic acid/water system.[12] Zhou and Powell extended the simulation to two-dimensions and three-dimensions on this basis, divided the simulation system into nonsolvent and polymer solutions, and described the formation of asymmetric-phase-separation morphology caused by interphase mass transfer through simulation.[13] In 2018, based on the Flory–Huggins theory, surface tension, and nonuniform density theory,[14] the formation of "sponge, finger, and layered" pore structures was simulated under different compositions and precipitation rates through two-dimensional simulations. However, the abovementioned phase-field models all assume constant mobility, which is unreasonable. The mobility changes and is affected by the concentration, which affects the phase-separation process. In 2021, Cervellere et al.[15] established the relationship between mobility and concentration, but their work simplified the three-component system into a two-component system, ignoring the mass transfer between a solvent and a nonsolvent, which would reduce the accuracy of the simulation.

Given the shortcomings of the above models, the phase-field model of the PVDF membrane system was optimized in this work. PVDF membranes are one of the most widely used membranes for ultrafiltration and microfiltration, and the membrane exhibits an asymmetric structure, which includes a nonporous, dense skin, and a porous structure.[16] The ternary Cahn–Hilliard (CH) equations and Flory–Huggins (1953) thermodynamic theory were used as the basis of the model, where the cross terms that have little effect on the system were ignored. According to the polymer macromolecular dynamics theory[17,18] and the experimental model proposed by Phillies,[19,20] a relationship between the mobility of a single molecule for each component in a nonsolvent (pure water) $D_i^0$, its self-diffusion coefficient $D_i$, and the concentration $c_i$ at the microscopic level were established, and the relationship between the mobility of solvent molecules and the mobility of solute molecules at the microscopic level was reasonably assumed. This improved the accuracy of the model and further refined and optimized the phase-field model. Finally, the relationship between $D_i^0$ and temperature was investigated.

Initial concentration fluctuations, changes in the initial PVDF concentration, and the mobility of different solvents were simulated because the initial concentration fluctuations had a certain effect on the skin layer but were difficult to observe in experiments according to the literature.[13] The solute concentration and solvent mobility played a vital role in the development of the skin layer and sublayer structure of the membrane prepared by the NIPS method,[21,22] and related experiments were compared with the model to verify its validity.

In the experimental section, PVDF solutes with different mass fractions and different solvents were used under the same conditions to conduct multiple sets of single-variable experiments. The simulations of initial concentration fluctuations were not verified by relevant experiments because the initial concentration fluctuations were related to the temperature, which was a complicated factor in the entire phase-transition process and not only affected the initial concentration fluctuations[23] but also had an impact on the thermodynamic and kinetic factors of the entire system. Therefore, it was difficult to reflect the influence of the initial concentration fluctuations on the phase-separation process experimentally, while simulations were able to overcome this issue.

## 2. MODEL

During immersion precipitation, the membrane forms through liquid–liquid phase separation first and then solidifies to a solid membrane. This work focuses on the membrane structure formed during the liquid–liquid demixing stage. Solidification is not considered here. A ternary Cahn–Hilliard formulation incorporating a Flory–Huggins homogeneous free-energy function is used as the basic governing equations. The governing equations are fourth-order partial differential equations.

According to the Flory–Huggins[24] theory, the Gibbs free energy ($\Delta G$) of a $p$ (polymer)/$s$ (solvent)/$n$ (nonsolvent) ternary system can be expressed as

$$\frac{\Delta G}{RT} = \left[\varphi_n \ln \varphi_n + \varphi_s \ln \varphi_s + \frac{\varphi_p}{m_p}\ln \varphi_p + \chi_{ns}\varphi_n\varphi_s + \chi_{sp}\varphi_s\varphi_p + \chi_{np}\varphi_n\varphi_p\right] \times (n_n + n_s + m_p n_p) \quad (1)$$

where $R$ is the gas constant, $T$ is the temperature, $n_i$ and $\varphi_i$ are the mole number and volume fraction of the component $i$, $m_p$ is the degree of polymerization of the polymer, and $\chi_{ij}$ is the Flory–Huggins interaction parameter ($i,j = p,s,n$).

The structural evolution of the ternary PVDF membrane system can be characterized by a binary volume fraction ($\phi_p$ and $\phi_s$) where there are two independent variables, which are equivalent to selecting two out of the three variables. $p$ and $s$ were chosen in this simulation. In a $p/s/n$ terpolymer membrane system, the same result would be obtained by choosing a nonsolvent with the correct parameters. The spatial evolution of the system can be obtained by solving the generalized Cahn–Hilliard[25] diffusion equation

$$\frac{\partial \varphi_p}{\partial t} = -\nabla J_p + \zeta_p \quad (2)$$

$$\frac{\partial \varphi_s}{\partial t} = -\nabla J_s + \zeta_s \quad (3)$$

where $\zeta_i$ is the thermal noise term described by the equation $\zeta_i^2 = \langle(\partial\varphi_i)^2\rangle$ in this study, which is the mean square error of component $i$, namely, the fluctuation intensity.[26] $Ji$ is the diffusion flux of component $i(i = p,s)$, based on the nonequilibrium thermodynamic theory proposed by Onsager,[27] which can be described by the chemical mobility and chemical potential gradient equations


https://dx.doi.org/10.1021/acsomega.0c05982
ACS Omega 2021, 6, 7444−7453

$$Jp = -M_{pp}\nabla(\mu_p - \mu_n) - M_{ps}\nabla((\mu_s - \mu_n) \tag{4}$$

$$Js = -M_{ss}\nabla(\mu_s - \mu_n) - Mps\nabla(\mu_p - \mu_n) \tag{5}$$

where $\mu s$, $\mu p$, and $\mu n$ are the chemical potentials of the components $s$, $p$, and $n$, respectively. $M_{ps}$ and $M_{sp}$ are the cross terms, which contribute relatively little to the entire system. Therefore, these terms are set to zero in most simulations.[13] $M_{ii}$ is the chemical mobility, which is closely related to the self-diffusion coefficient, $D_i$, where $(i = p, s)$[28]

$$M_{pp} = \frac{Dp}{\frac{\partial^2 f}{\partial \varphi_p^2}} \tag{6}$$

$$M_{ss} = \frac{Ds}{\frac{\partial^2 f}{\partial \varphi_s^2}} \tag{7}$$

where $f$ is the body free-energy density (free energy per mole). According to eq 1, the following equation can be obtained

$$f = \frac{RT}{Vm}\left(\varphi_n \ln \varphi_n + \varphi_s \ln \varphi_s + \frac{\varphi_p}{mp}\ln \varphi_p + \chi_{ns}\varphi_n\varphi_s + \chi_{sp}\varphi_s\varphi_p + \chi_{np}\varphi_n\varphi_p\right) \tag{8}$$

where $Vm$ is the molar volume of the ternary system.

The model verified by Phillies[19,20] was used to describe the relationship between $D_i$ and $\phi_i$ $(i = p,s)$

$$D_i = D_i^0 \exp(-\alpha(c_i)^{\nu}) \tag{9}$$

where $^0_i$ is the diffusion rate of a single molecule of the component $i$ in pure water and $c$ is the concentration (g/L) of component $i(i = p,s)$, which can be expressed as $c_i = \phi_i \frac{M_i^v}{M_i^w}$. $M_i^v$, $M_i^w$ are the molar volume and molar mass of component $i$, respectively, where $M_p^v = 38.2\frac{\text{mL}}{\text{mol}}$, $M_p^w = 64.03\frac{\text{g}}{\text{mol}}$ for the PVDF monomer. $\alpha$ and $\nu$ are the relevant parameters of the system; we choose the polymer system parameters 0.2 and 0.4 within a reasonable range for this simulation.[19,20]

$D_s^0$ is chosen to be 1000 times of $D_p^0$ to capture the relative difference of the mobilities of the polymer and the small molecule since the diffusivity of small molecules is typically $10^{-6}$ cm$^2$/s and the diffusivity of polymers is about typically $10^{-9}$ cm$^2$/s.[29−32] Therefore, for polymers, $D_p^0 = 10$. For different solvents, $D_S^0 = D_m \times 10^{-12}$ was taken to describe the diffusion rate of solvent molecules in pure water at the microscopic level. $D_m$ is the solvent/nonsolvent ($H_2O$) mutual diffusion coefficient, which was used to describe the diffusion rate of the solvent in the nonsolvent ($H_2O$).

According to the Einstein equation, $D_i^0$ can be expressed as

$$D_i^0 = \frac{k_b T}{\eta} \tag{10}$$

where $\eta$ is the friction factor, $k_b$ is the Boltzmann constant, and $T$ is the temperature. According to eqs 9 and 10, $D_i(i = p,s)$ is directly related to temperature and concentration.

The difference between the chemical potential of substances $i$ and $j$, $(\mu_i - \mu_j)$, is equal to the differential of the local total free energy $G$ with respect to the local volume fraction $\varphi_i$

$$\frac{\delta G}{\delta \varphi_p} = (\mu_p - \mu_n) \tag{11}$$

$$\frac{\delta G}{\delta \varphi_s} = (\mu_s - \mu_n) \tag{12}$$

According to Zhou,[13] eqs 11 and 12 can be expressed as

$$\mu_p - \mu_n = \frac{\delta f}{\delta \varphi_p} - K_{pp}\nabla^2\varphi_p - \frac{1}{2}(K_{sp} + K_{ps})\nabla^2\varphi_s \tag{13}$$

$$\mu_s - \mu_n = \frac{\delta f}{\delta \varphi_s} - K_{ss}\nabla^2\varphi_s - \frac{1}{2}(K_{sp} + K_{ps})\nabla^2\varphi_p \tag{14}$$

where $K_{ij}$ is the gradient penalty coefficient.

In summary, the governing equations can be expressed as follows

$$\frac{\partial \varphi_p}{\partial_t} = \nabla\left[\frac{Dp}{\frac{\partial^2 f}{\partial \varphi_p^2}}\nabla\left(\frac{\delta f}{\delta \varphi_p} - K_{pp}\nabla^2\varphi_p - \frac{1}{2}(K_{sp} + K_{ps})\nabla^2\varphi_s\right)\right] + \zeta_p \tag{15}$$

$$\frac{\partial \varphi_s}{\partial_t} = \nabla\left[\frac{Ds}{\frac{\partial^2 f}{\partial \varphi_s^2}}\nabla\left(\frac{\delta f}{\delta \varphi_s} - K_{ss}\nabla^2\varphi_s - \frac{1}{2}(K_{sp} + K_{ps})\nabla^2\varphi_p\right)\right] + \zeta_s \tag{16}$$

To calculate the efficiency and verify the versatility, eqs 15 and 16 were transformed into the dimensionless forms, eqs 17 and 18

$$\frac{\partial \varphi_p}{\partial t^*} = \nabla^*\left[\frac{D_p^*}{\frac{\partial^2 f}{\partial \varphi_p^2}}\nabla^*\left(\frac{\delta f}{\delta \varphi_p} - K_{pp}^*\nabla^{*2}\varphi_p - \frac{1}{2}(K_{sp}^* + K_{ps}^*)\nabla^{*2}\varphi_s\right)\right] + \zeta_p^* \tag{17}$$

$$\frac{\partial \varphi_s}{\partial t^*} = \nabla^*\left[\frac{D_s^*}{\frac{\partial^2 f}{\partial \varphi_s^2}}\nabla^*\left(\frac{\delta f}{\delta \varphi_s} - K_{ss}^*\nabla^{*2}\varphi_s - \frac{1}{2}(K_{sp}^* + K_{ps}^*)\nabla^{*2}\varphi_p\right)\right] + \zeta_s^* \tag{18}$$

where the dimensionless parameters are as follows

$$\nabla^* = \left[\frac{\partial}{\partial\left(\frac{x}{l^{*2}}\right)}, \frac{\partial}{\partial\left(\frac{y}{l^{*2}}\right)}\right], K_{ij}^* = \frac{K_{ij}}{\frac{l^{*2}RT}{V_m}}, D_i^* = \frac{D_i}{\frac{RT}{V_m}}(i, j = p, s) \tag{19}$$



https://dx.doi.org/10.1021/acsomega.0c05982
ACS Omega 2021, 6, 7444−7453

where $(x,y)$ is the coordinate in the two-dimensional simulation plane and $l^*$ is the length unit.

In the simulation, the ratio of the $x$ dimension to the y dimension is 1:2, and the grid size is set to 200 × 400. The grid spacing $\Delta x = 0.1 \times l^*$ and the time step size is $\Delta t = 0.1 \times t^*$. $L$ is the width of the domain in the two dimension. Width, in turn, is chosen to be roughly 10−20 times the initial spinodal decomposition wavelength to efficiently approach the limit of an infinite system while using periodic boundary conditions. The pore size in PVDF is average about 100 nm, which is half of one spinodal wavelength. There is averagely 10−20 times the initial spinodal decomposition wavelength in the simulations. Therefore, the simulation domain is about $L$ = 2−4 $\mu$m. Taking the average value, $L$ = 3$\mu$m. The final simulation box size is 3 × 6 $\mu m^2$, the length and time unit are $l^* = \frac{L}{200} = 15$ nm and $t^* = \frac{l^{*2}}{10^{-9}\,\mathrm{cm/s^2}} = 2.3 \times 10^{-6}$ s, respectively.

## 3. EXPERIMENTAL SECTION

**3.1. Materials and Reagents.** PVDF (FR904) was purchased from Shanghai 3F New Material Co. Ltd., China.

**Table 1. Chemical Compounds**

| chemical name | chemical or linear formula | CAS number | density ($g/cm^3$) |
|---|---|---|---|
| $H_2O$ | $H_2O$ | 7732-18-5 | 1 |
| PVDF | $-(C_2H_2F_2)_n-$ | 24937-79-9 | 1.77 |
| DMSO | $C_2H_6OS$ | 67-68-5 | 1.100 |
| DMAc | $C_4H_9NO$ | 127-19-5 | 0.937 |
| DMF | $C_3H_7NO$ | 68-12-2 | 0.945 |

**Table 2. Composition Table for Each Component**

| case | PVDF (wt %) | solvent type | solvent (wt %) | nonsolvent (wt %) |
|---|---|---|---|---|
| S0 | 0.10 | DMSO | 0.80 | 0.10 |
| S1 | 0.15 | DMSO | 0.75 | 0.10 |
| S2 | 0.20 | DMSO | 0.70 | 0.10 |
| S3 | 0.10 | DMAc | 0.80 | 0.10 |
| S4 | 0.10 | DMF | 0.80 | 0.10 |

*N*,*N*-dimethylformamide (DMF), *N*,*N*-dimethylacetamide (DMAc), and dimethyl sulfoxide (DMSO) were purchased from Tianjin Jiangtian Chemical Company, which were all analytical grade, and the detailed chemical compounds are shown in Table 1.

**3.2. Preparation and Characterization of Flat PVDF Microporous Membranes.** To verify the accuracy of the model, the experiments were divided into five groups, as shown in Table 2.

PVDF was dried in an oven at 60 °C for 24 h to remove excess water before the experiments. The solvent and deionized water were added in a proper ratio (10:1) to an Erlenmeyer flask and ultrasonically dispersed. A certain amount of PVDF was weighed and placed in the mixed solution to obtain the desired 0.10, 0.15, and 0.20 volume fractions for different solvents DMSO, DMAc, and DMF, and stirred at 60 °C for 10 h until it was completely dissolved. The mixture was kept in a 60 °C water bath for 12 h to defoam. Next, the casting liquid was cast on a glass plate and scraped with a scraper to make a solution membrane (choose a thickness of 200 $\mu$m), and it quickly immersed in a pure water solution at room temperature for phase inversion. The water was changed every 8 h during the first 3 days (72 h) and changed every day for the following 4 days. After 7 days, phase inversion of the membrane was considered complete, and the membrane was stored in pure water for later use.

The crystal structure and crystallinity of the membrane were characterized by a wide-angle X-ray diffractometer (Rigaku, Dnax-rA). The morphology and structure of the top and bottom surfaces and the end face of the membrane were characterized using a field-emission scanning electron microscope (SEM, DSa100, Hitachi, Japan). The density method was used to determine the porosity of the PVDF membrane,[31] and the details were as follows: a certain area of the dried PVDF membrane was weighed on an electronic balance, and the thickness of the membrane was measured with an optical microscope (6XBPC, Shanghai Optical Instrument Factory, with an accuracy of 0.01 mm). The volume and density ($\rho_m$) of the membrane were calculated and the porosity ($\varepsilon$) of the membrane was determined using the equation $\varepsilon = (1 - \rho_m/\rho_p) \times 100\%$, where $\rho_p$ is the density of PVDF (1.77 $g/cm^3$).

## 4. RESULTS AND DISCUSSION

We used the Anaconda 3.0 program to numerically solve eqs 17 and 18 (for more program settings, please contact the author). The cross-gradient penalty coefficients ($K^*_{ss}$ and $K^*_{pp}$) were ignored in the simulation, and the same constant that was estimated by Caneba[12] was used to set the values of $K^*_{ss}$ and $K^*_{pp}$. During the numerical calculation process, the following parameters were used: $K^*_{ss} = K^*_{pp} = 1.8 \times 10^{-6}$, $V_m = 1.8 \times 10^{-5}$ $m^3$/mol, $R$ = 8.314 J/K/mol, $m_p$ = 50.

Under the condition of $T$ = 60 °C, according to Zhou,[14] the Flory−Huggins interaction parameter of the DMF solvent system is: $\chi_{ns}$ = 0.2, $\chi_{sp}$ = 0.3, and $\chi_{np}$ = 1; according to Shuguang,[33] the Flory−Huggins interaction parameter of the DMAc solvent system is: $\chi_{ns}$ = 0.4, $\chi_{sp}$ = 0.4, and $\chi_{np}$ = 1.2; according to Yilmaz,[34] the Flory−Huggins interaction parameter of the DMSO solvent system is: $\chi_{ns}$ = 0.5, $\chi_{sp}$ = 0.6, and $\chi_{np}$ = 1.4.

The domain size for the two-dimensional simulation is 3 × 6 $\mu m^2$ (resolved with a 200 × 400 grid). A combination of 30% membrane-forming liquid and 70% gel bath was used in the simulations, and $\varphi_p$ and $\varphi_s$ were equal to 0.01 in the gel bath. Periodic boundary conditions were applied in the x direction and symmetric boundary conditions were used in the $y$ direction. At the end of the simulation, the computer scans the proportion of the polymer-rich phase in the gel domain to calculate the porosity of the simulated sample. In the repeated simulation work, we choose the time point at which the whole system begins to stabilize in the simulations as the termination of the simulations, which can be used to approximate the time of phase separation.

In Sections 4.1 and 4.2, the effects of the initial concentration difference of PVDF and the concentration fluctuation on the skin layer and sublayer structures of the membrane in the PVDF/DMSO/$H_2O$ ternary system were simulated. In Section 4.3, the effects of the diffusion rates of different solvents on the PVDF membrane skin layer and sublayer structures were simulated.

**4.1. Effect of the Initial PVDF Concentration on the Skin Layers and Sublayers.** To study the effect of the initial PVDF concentration on the evolution of the skin layer and sublayer structures, several initial concentrations were chosen to be simulated under the same conditions. Figure 1 shows the microscopic simulation diagrams of the ternary PVDF


https://dx.doi.org/10.1021/acsomega.0c05982
ACS Omega 2021, 6, 7444−7453

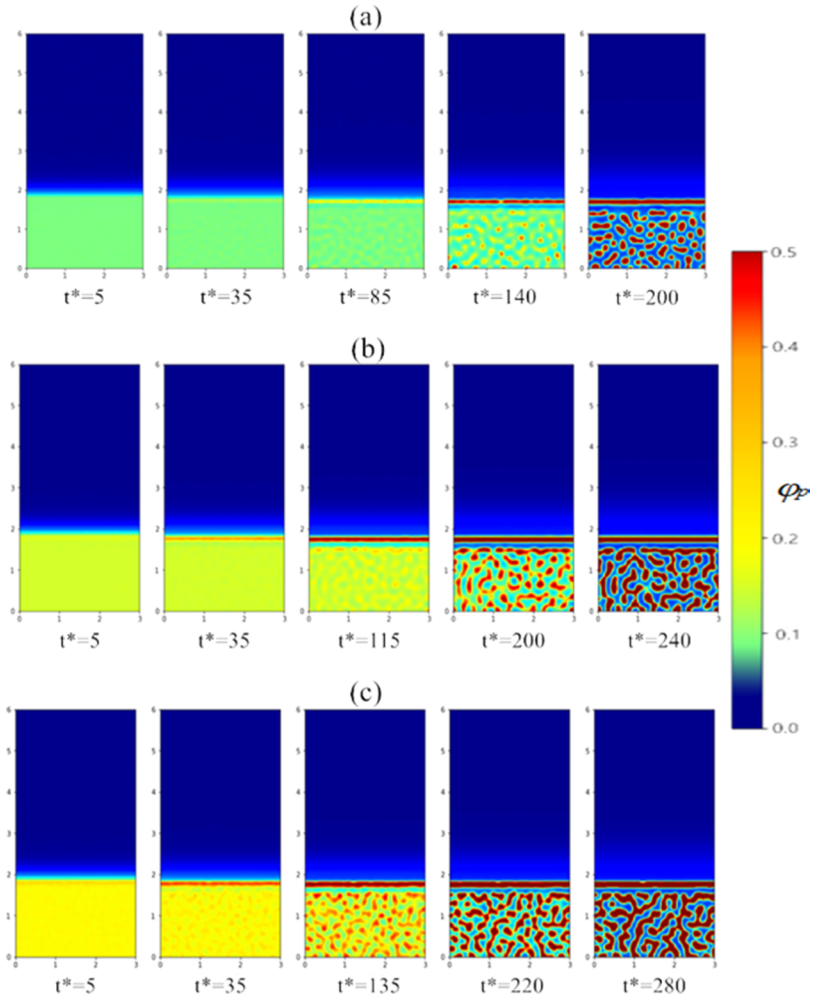


**Figure 1.** Microscopic simulation diagrams of ternary PVDF membrane systems at different times with a concentration fluctuation of $10^{-3}$ at different initial concentrations of PVDF (a, b, c).

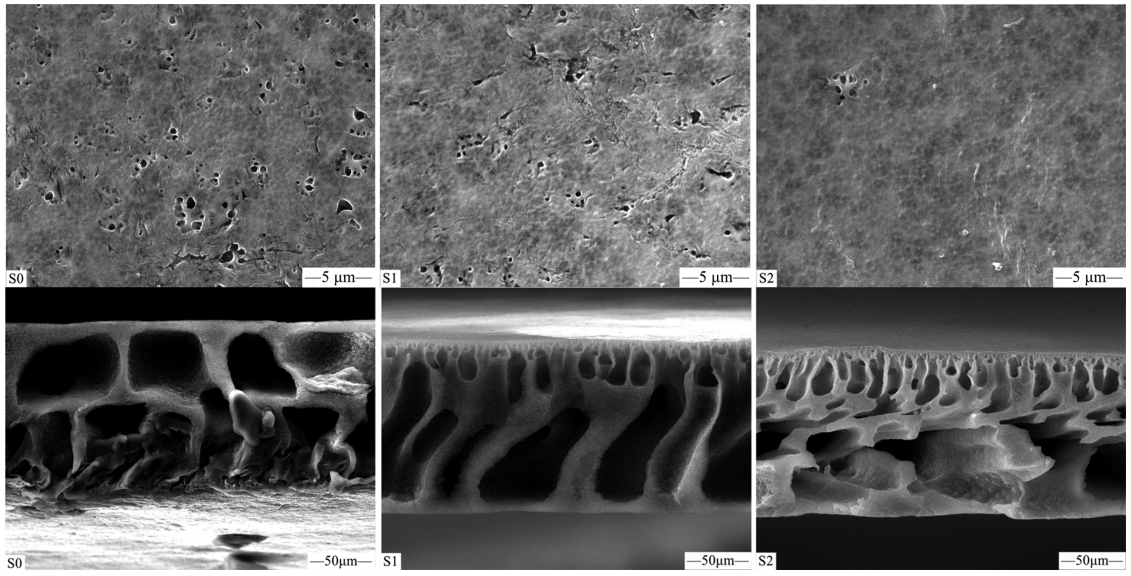


**Figure 2.** SEM images of membrane cross sections with different initial concentrations of PVDF (S0, S1, and S2).

membrane systems with different initial PVDF concentrations (a: $\varphi_p$ = 0.10, $\varphi_s$ = 0.80; b: $\varphi_p$ = 0.15, $\varphi_s$ = 0.75; c: $\varphi_p$ = 0.20, and $\varphi_s$ = 0.70) when the initial concentration fluctuation ($\zeta^*$) was equal to $10^{-3}$. Figure 2 shows the SEM images of the membrane cross sections with different initial PVDF concentrations (S0, S1, and S2). Figure 3 shows the porosities



https://dx.doi.org/10.1021/acsomega.0c05982
ACS Omega 2021, 6, 7444−7453

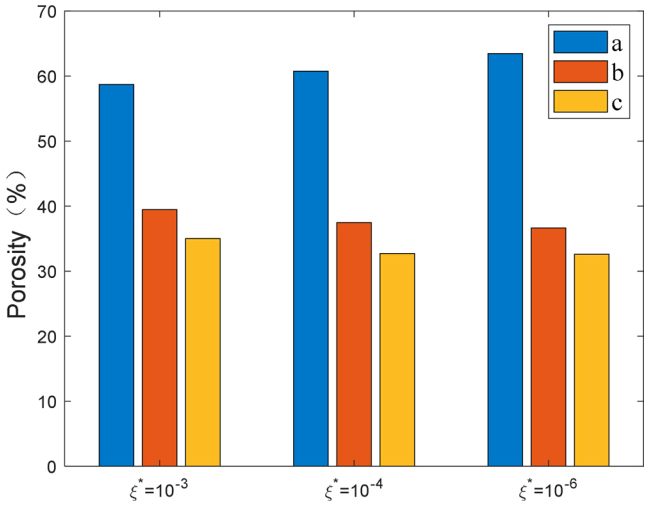


**Figure 3.** Porosity of different initial PVDF concentrations (a, b, c) in different initial concentration fluctuations ($\zeta^*$) in the simulation.

of the membranes with different initial PVDF concentrations (a, b, and c) and $\zeta^*$ in the simulations. Table 3 displays the measured porosities and crystallinities after the membrane formation of each component. It was observed that the simulation results were consistent with the experimental results. The driving force of the initial phase change became larger and the appearance of the skin layer became faster as the PVDF concentration increased, leading to a decreased permeability, smaller pore sizes, and a smaller porosity of the membrane. This resulted in reduced water permeability yet had little effect on the number of skin layers. These changes in the structure and performance were consistent with previous studies.[32,35]

**Table 3. Porosities and Crystallinities of Different Components after Membrane Formation in the Experiments**

| sample | porosity (%) | crystallinity (%) |
|---|---|---|
| S0 | 79.8 | 18.6 |
| S1 | 55.8 | 43.5 |
| S2 | 51.4 | 51.5 |
| S3 | 70.2 | 22.5 |
| S4 | 65.4 | 25.1 |

The skin layer mainly underwent liquid−liquid instantaneous phase separation when the concentration of PVDF was low, forming a poor phase and rich phase, which hardly hindered the mass transfer between the sublayers and the coagulation bath. Therefore, the mass transfer between the solvent and coagulation bath in the sublayers was still rather

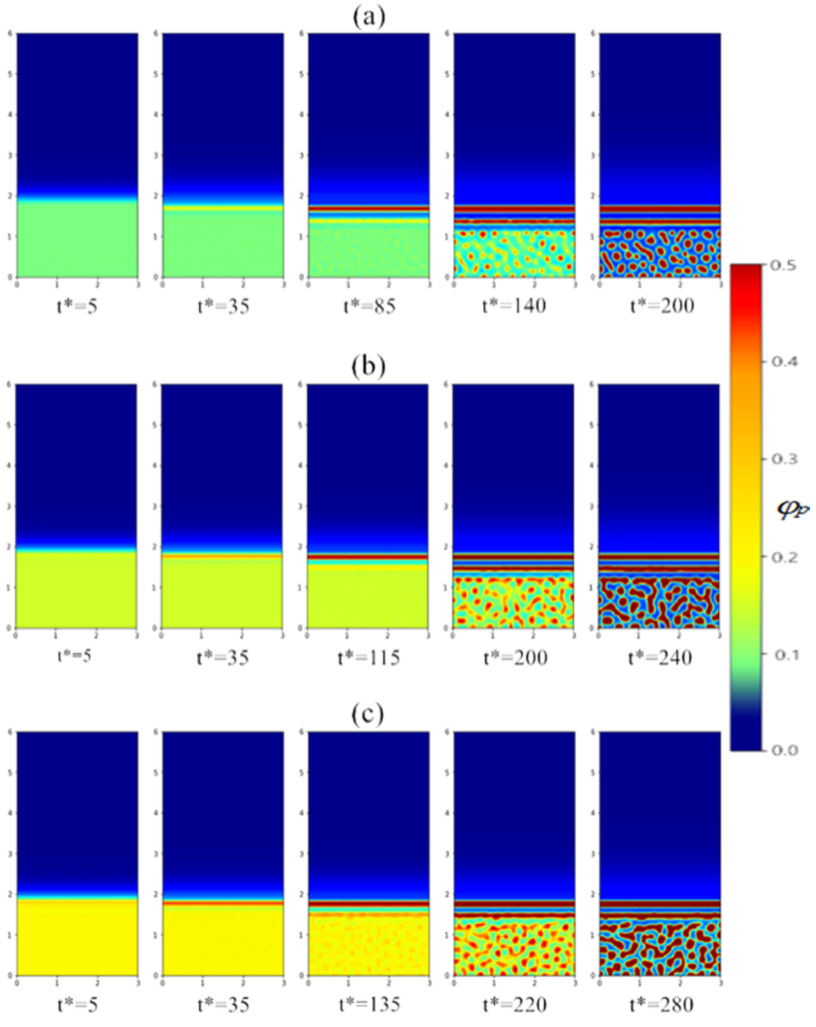


**Figure 4.** Microscopic simulation diagrams of ternary PVDF membrane systems at different times with a concentration fluctuation of $10^{-4}$ at different initial concentrations of PVDF (a−c).



https://dx.doi.org/10.1021/acsomega.0c05982
ACS Omega 2021, 6, 7444−7453

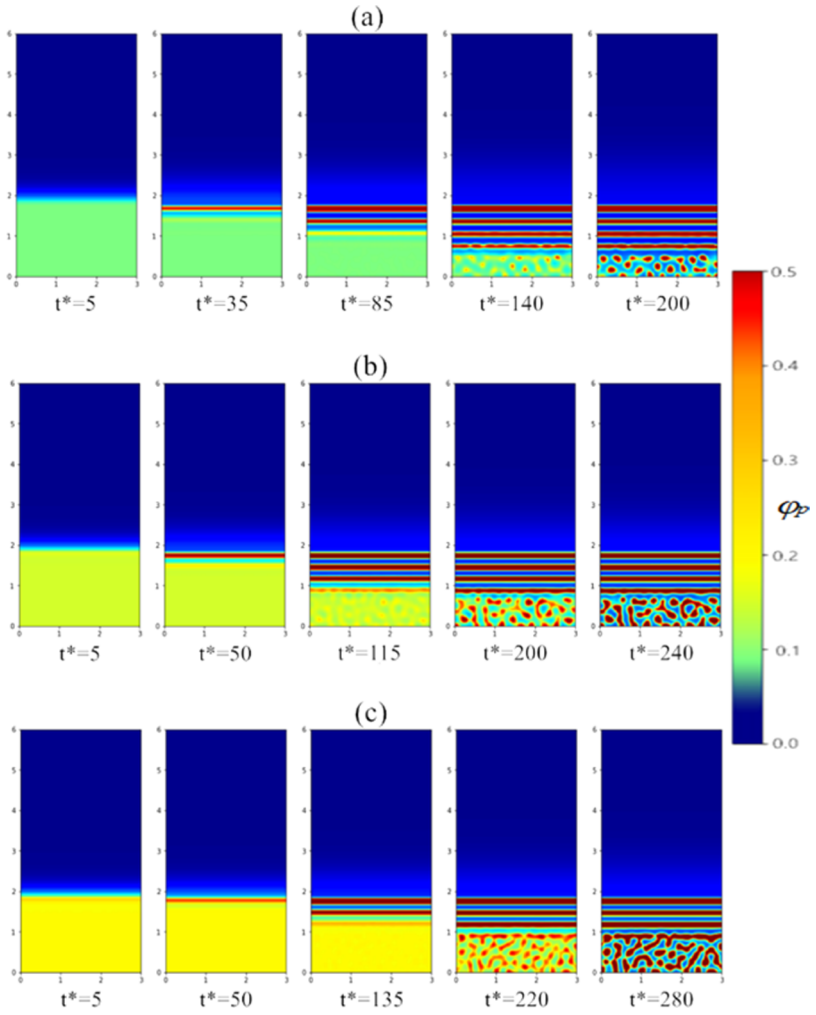


**Figure 5.** Microscopic simulation diagrams of ternary PVDF membrane systems at different times with a concentration fluctuation of $10^{-6}$ at different initial concentrations of PVDF (a–c).

rapid, causing the entire sublayer to quickly enter the liquid–liquid phase-separation zone. Subsequently, liquid–liquid phase separation occurred, and continuous rich phases and dispersed poor phases were generated. According to the "advantage of first nucleus growth" and macropore development theories proposed by Strathmann,[6,36] the poor-phase nuclei first generated below the skin layer had "growth advantages" over the latter nuclei due to the strong interaction of the solvent/nonsolvent pairs and the rapid diffusion rate. These poor-phase nuclei can be regarded as small coagulation baths, and most of the nonsolvent diffusing into the sublayers through the skin layer and the solvent diffusing out of the rich phase diffused into the nuclei to make them grow, merge, and develop into macropores. For low-polymer-concentration systems, the polymer had poor crystallinities and fast diffusion rates, and instantaneous liquid–liquid phase separation occurred in the sublayers. The phase separation time was short, and finally, the sublayer sublayer macroporous void structure was obtained. When the concentration of PVDF was high, the casting liquid at the interface tended to undergo liquid–solid phase separation, and the separation of the skin layer had an obstructive effect on the mass transfer. The decrease in the amount of the sublayer solvent diffusing into the coagulation bath made the polymer concentration of the sublayer almost unchanged at first, which weakened the macropore development and delayed the phase-separation behavior in the sublayers. The sublayers transformed from transient liquid–liquid phase separation to delayed liquid–liquid phase separation. Hence, the phase-separation time became longer, the macropores in the sublayer structure decreased, and the sponge-like structures increased, leading to the decrease of the porosity and flux of the membrane.

**4.2. Effects of the Initial Concentration Fluctuation on the Skin Layers and Sublayers.** To understand the effect of initial concentration fluctuations on the structure of the skin layers and sublayers, different $\zeta^*$s were simulated under the same conditions, as shown in Figures 1–5.

Simulations showed a layered structure in the early stage of the immersion precipitation process. The number of layers varies with the initial fluctuation $\zeta^*$ to the polymer mobility. Then, these layers merged into bulk membranes due to the coarsening. So it is hard to observe in the experiment. The time of membrane formation became longer with increasing the number of skin layers, but the change in $\zeta^*$ had a little effect on the porosity of the membrane and the structure of the sublayers.

This may be because the free-energy gradient in the $y$-direction was relatively reduced with the increase of the initial concentration fluctuations, which led to a decrease in the relative delamination strength for the skin layers, and thus the


https://dx.doi.org/10.1021/acsomega.0c05982
ACS Omega 2021, 6, 7444–7453

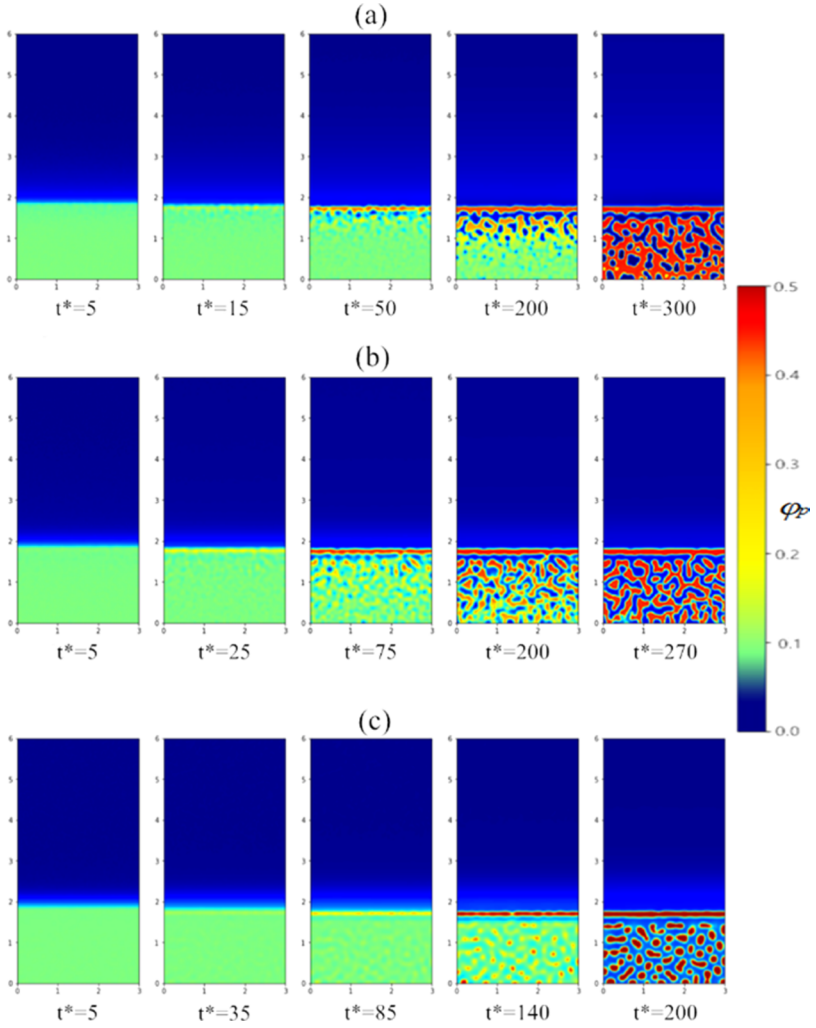


**Figure 6.** Microscopic simulation diagram of ternary PVDF membrane systems with different solvents: (a) DMF, (b) DMAc, and (c) DMSO.

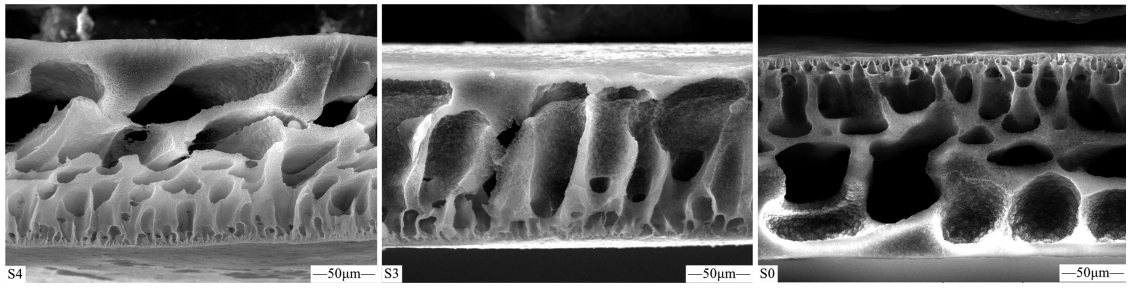


**Figure 7.** SEM images of PVDF membrane cross sections with different solvents: (S4) DMF, (S3) DMAc, and (S0) DMSO.

number of layers was correspondingly reduced, which was shown in the simulations with different initial concentration fluctuations. This means that if there are large random fluctuations in the system (e.g., high temperature), the membrane system will likely form a spinodal morphology more uniformly throughout the polymer solution without the formation of layers.

**4.3. Effects of Solvent Diffusion Rates on the Skin Layers and Sublayers.** To study the influence of the solvent diffusion rates on the structure of the skin layers and sublayers, different diffusion rates of the solvents in the nonsolvent were simulated under the same conditions, as shown in Figure 6. Different solvent systems (DMSO, DMAc, and DMF) were chosen for this experiment, and the mobilities ($D_m$) increased in the order of DMSO ($8.4 \times 10^6$ cm$^2$/s), DMAc ($11.4 \times 10^6$ cm$^2$/s), and DMF ($12.8 \times 10^6$ cm$^2$/s) by Bottino[22] and Wilke.[37] Figure 7 shows SEM images of the different solvent systems. The morphology of DMAc and DMF does not change much, as shown in Figure 7, because the mobility ($D_m$) gap between them is small, which is consistent with the simulated changing trend. The sublayers gradually changed from sublayer macroporous void structures to sponge-like pore structures as the solvent mobility decreased, leading to a larger porosity, which was consistent with the simulation results. Figure 8 shows the relationship between porosity and time in the transition-phase process in the different systems during the


https://dx.doi.org/10.1021/acsomega.0c05982
ACS Omega 2021, 6, 7444−7453

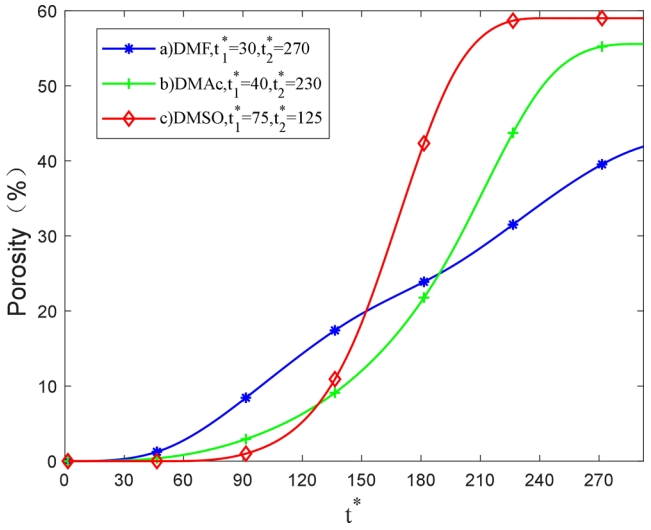


**Figure 8.** Change in the porosity of membranes formed in different solvents during the simulation.

simulation. The delay time of the skin liquid−solid phase separation ($t1$) decreased as the phase separation time ($t2$) increased.

This may be due to the decrease of the solvent diffusion rate, which led to an increased delay time of the liquid−solid phase separation ($t1$) for the skin layers. The formation of the skin layers hindered the mutual mass transfer between the sublayers and the coagulation bath, that is, the amount of nonsolvent diffusing into the sublayers was greater than that of the solvent diffusing out of the sublayers. The solvent loss in the sublayers was rather small at the beginning and the polymer concentration was almost unchanged, and a part of the composition below the skin layers quickly entered the liquid−liquid phase-separation zone, forming a polymer-poor phase and a polymer-rich phase. Hence, the poor-phase nuclei were distributed in the continuous rich phase. As the nonsolvent further diffused into the sublayers, the growth of the already-generated nuclei and the generation and growth of the new nuclei in the casting liquid below the sublayers occurred simultaneously. According to the advantage of first nucleus growth theory,[32] the growth of the already-generated nuclei and the new nuclei both consumed the nonsolvent, resulting in a competitive relationship. The amount of the nonsolvent entering the sublayers was greater than of the solvent diffusing out since the phase separation of the skin layers was slow, and these nonsolvents all entered the already-generated poor-phase nuclei. The amount of nonsolvent in the poor-phase nuclei that diffused into the casting liquid at the nuclei front was low due to the high viscosity and the slow diffusion rate of the casting liquid at the nuclei front, and most of the nonsolvent remained in the already-generated poor-phase nuclei. This indicated that the growth of the generated nuclei was much faster than that of the newly formed nuclei. According to the macropore development theory,[38] these generated nuclei with growth advantage can be regarded as small coagulation baths, and most of the nonsolvent diffused into the sublayers through the skin layers and the solvent diffused out of the rich phase and into the nuclei to make them grow and merge. The poor phase dispersed in the rich phase can hardly grow due to the rapid phase-separation process, and hence a sponge-like pore structure was formed. However, the number of new nuclei generated in the system cannot be ignored as the diffusion rate increased, which limited the development of the already-generated nuclei into macropores. Therefore, the advancement speed of the gel front slowed down and the phase-separation speed ($t_2$) decreased.

## 5. CONCLUSIONS

The simulation results were compared with the experimental results, and the following conclusions were obtained:

(1) In the simulations, the skin layers grew fast, and the number of sponge-like pores in the sublayers increased for high PVDF concentrations, which was due to the crystallization behavior of the polymer. The crystallinity of high polymer concentrations would slow down the speed of phase separation, and the sublayers transformed from instantaneous liquid−liquid phase separation to delayed liquid−liquid phase separation. The phase separation time increased, leading to an increase of sponge-like pores in the sublayers.

(2) Increasing the initial concentration fluctuation relatively reduced the free-energy gradient in the y-direction, thereby reducing the delamination strength and the number of skin layers, but had little effect on the sublayer structure.

(3) The phase separation of the skin layers was controlled by the thermodynamic properties of the system, mainly by the delayed liquid−solid phase separation. The delay time was controlled by the diffusion kinetics, which decreased with the increase of the diffusion rate. Short sublayer phase separation times (instantaneous phase separation) were conducive to the development of macropores, and long phase separation times (delayed phase separation) were conducive to the formation of sponge-like pore structures. The simulation and experimental results were consistent, which verified the validity of the model.

In the next step, the connection between a microscopic or mesoscopic model and the phase-field model for the PVDF membrane system will be established to obtain accurate thermodynamic parameters, further deepening the understanding of the phase-separation process.

## AUTHOR INFORMATION


### Corresponding Author

**Chaoyu Yang** − *School of Urban Planning and Municipal Engineering, Xian Polytechnic University, Xi'an 710048, Shanxi, China*; orcid.org/0000-0001-8758-8852; Email: 416272701@qq.com

### Authors

**Ping Fang** − *School of Urban Planning and Municipal Engineering, Xian Polytechnic University, Xi'an 710048, Shanxi, China*

**Ruihua Shao** − *School of Environmental and Chemical Engineering, Xian Polytechnic University, Xi'an 710048, Shanxi, China*

**Lihui Zhou** − *Oil and Gas Technology Research Institute, Changqing Oil Field Company, Xi'an 710055, Shanxi, China*

**Kang Liu** − *School of Urban Planning and Municipal Engineering, Xian Polytechnic University, Xi'an 710048, Shanxi, China*

Complete contact information is available at:




https://dx.doi.org/10.1021/acsomega.0c05982
ACS Omega 2021, 6, 7444−7453

https://pubs.acs.org/10.1021/acsomega.0c05982

### Notes

The authors declare no competing financial interest.

## ■ ACKNOWLEDGMENTS

The authors would like to acknowledge School of Urban Planning and Municipal Engineering of Xi'an Polytechnic University for providing experimental equipment. The authors would like to acknowledge mentors from the Changqing Oil Field Company and the Xi'an Polytechnic University for their guidance and insight on the direction of the project.

## ■ REFERENCES

(1) Wang, D. M.; Lai, J. Y. Recent advances in preparation and morphology control of polymeric membranes formed by nonsolvent induced phase separation. *Curr. Opin. Chem. Eng.* **2013**, *2*, 229−237.
(2) Kim, J. F.; Kim, J. H.; Lee, Y. M.; Drioli, E. Thermally induced phase separation and electrospinning methods for emerging membrane applications: A review. *AIChE J.* **2016**, *62*, 461−490.
(3) Liu, M.; Liu, S. H.; Xu, Z. L.; Wei, Y. M.; Yang, H. Formation of micro-porous polymeric membranes via thermally induced phase separation: A review. *Front. Chem. Sci. Eng.* **2016**, *10*, 57−75.
(4) Yang, X.; Wang, R.; Shi, L.; Fane, A. G.; Debowski, M. Performance improvement of PVDF hollow fiber-based membrane distillation process. *J. Membr. Sci.* **2011**, *369*, 437−447.
(5) Mulder, M. *Basic Principle of Membrane Technology*; Kluwer Academic Publishers: The Netherlands, 1992; pp 1−26.
(6) Strathmann, H.; Koch, K. The formation mechanism of phase inversion membranes. *Desalination* **1977**, *21*, 241−249.
(7) Altena, F. W.; Smolders, C. A. Calculation of liquid-liquid phase separation in a ternary system of a polymer in a mixture of a solvent and a nonsolvent. *Macromolecules* **1982**, *15*, 1491−1497.
(8) Broens, L.; Koenhen, D. M.; Smolders, C. A. On the mechanism of formation of asymmetric ultra-and hyper-filtration membranes. *Desalination* **1977**, *22*, 205−219.
(9) Mulder, M. H. V.; Henderikman, J. O.; Wijnans, J. G.; Smolders, C. A. A rationale for the preparation of asymmetric pervaporation membrane. *J. Appl. Polym. Sci.* **1985**, *30*, 2805−2820.
(10) Wijmans, J. G.; Baaij, J. P. B.; Smolders, C. A. The mechanism of formation of microporous or skinned membranes produced by immersion precipitation. *J. Membr. Sci.* **1983**, *14*, 263−274.
(11) Tsay, C. S.; McHugh, A. J. Mass transfer modeling of asymmetric membrane formation by phase inversion. *J. Polym. Sci., Part B: Polym. Phys.* **1990**, *28*, 1327−1365.
(12) Saxena, R.; Caneba, G. Studies of spinodal decomposition in a ternary polymer-solvent-nonsolvent system. *Polym. Eng. Sci.* **2002**, *42*, 1019−1031.
(13) Zhou, B.; Powell, A. C. Phase field simulations of early stage structure formation during immersion precipitation of polymeric membranes in 2D and 3D. *J. Membr. Sci.* **2006**, *268*, 150−164.
(14) Hopp-Hirschler, M.; Nieken, U. Modeling of pore formation in phase inversion processes: Model and numerical results. *J. Membr. Sci.* **2018**, *564*, 820−831.
(15) Cervellere, M. R.; Qian, X.; Ford, D. M.; et al. Phase-field modeling of non-solvent induced phase separation (NIPS) for PES/NMP/Water with comparison to experiments. *J. Membr. Sci.* **2021**, *619*, No. 118779.
(16) Akthakul, A. Design of Chemistry and Morphology of Polymer Filtration Membranes. Ph.D. Thesis; MIT, 2003.
(17) Hoogerbrugge, P. J.; Koelman, J. M. V. A. Simulating microscopic hydrodynamic phenomena with dissipative particle dynamics. *Europhys. Lett.* **1992**, *19*, 155−160.
(18) Chen, L. Q. Computer simulation of spinodal decomposition in ternary systems. *Acta Metall. Mater.* **1994**, *42*, 3503−3513.
(19) Phillies, G. D. J. Universal scaling equation for self-diffusion by macromolecules in solution. *Macromolecules* **1986**, *19*, 2367−2376.
(20) Phillies, G. D. J. The hydrodynamic scaling model for polymer self-diffusion. *J. Phys. Chem. A* **1989**, *93*, 5029−5039.
(21) Cheng, L. P.; Dwan, A. H.; Gryte, C. C. Membrane formation by isothermal precipitation in polyamide-formic acid-water systems I. Description of membrane morphology. *J. Polym. Sci., Part B: Polym. Phys.* **1995**, *33*, 211−222.
(22) Bottino, A.; Camera-Roda, G.; Capannelli, G.; Munari, S. The formation of microporous polyvinylidene difluoride membranes by phase separation. *J. Membr. Sci.* **1991**, *57*, 1−20.
(23) Young, T. H.; Cheng, L. P.; You, W. M.; Chen, L. Y. Prediction of EVAL membrane morphologies using the phase diagram of water−DMSO−EVAL at different temperatures. *Polymer* **1999**, *40*, 2189−2195.
(24) Flory, H. *Principles of Polymer Chemistry*; Cornell University Press: Ithaca, 1953.
(25) Cahn, J.; Hilliard, J. E. Free Energy of a Nonuniform System. I. Interfacial Free Energy. *J. Chem. Phys.* **1958**, *28*, 258−267.
(26) Abe, T. Thermal equilibrium concentration fluctuations above the critical temperature in a Ni-Cu alloy. *Acta Metall. Mater.* **1992**, *40*, 1951−1959.
(27) Onsager, L. Reciprocal relations in irreversible processes. II. *Phys. Rev.* **1931**, *38*, No. 2265.
(28) Barton, B. F.; Graham, P. D.; McHugh, A. J. Dynamics of spinodal decomposition in polymer solutions near a glass transition. *Macromolecules* **1998**, *31*, 1672−1679.
(29) Bartels, C. R.; Crist, B.; Graessley, W. W. Self-diffusion coefficient in melts of linear polymers: chain length and temperature dependence for hydrogenated polybutadiene. *Macromolecules* **1984**, *17*, 2702−2708.
(30) Cheng, L. P.; Lin, D. J.; Shin, C. H.; Dwan, A. H.; Gryte, C. C. PVDF membrane formation by diffusion-induced phase separation-morphology prediction based on phase behavior and mass transfer modeling. *J. Polym. Sci., Part B: Polym. Phys.* **1999**, *37*, 2079−2092.
(31) Kim, J. H.; Min, B. R.; Park, H. C.; Won, J.; Kang, Y. S. Phase behavior and morphological studies of polyimide/PVP/solvent/water systems by phase inversion. *J. Appl. Polym. Sci.* **2001**, *81*, 3481−3488.
(32) Kim, Y. D.; Kim, J. Y.; Lee, H. K.; Kim, S. C. A new modeling of asymmetric membrane formation in rapid mass transfer system. *J. Membr. Sci.* **2001**, *190*, 69−77.
(33) Shuguang, L.; Chengzhang, J.; Yuanqi, Z. The investigation of solution thermodynamics for the polysufone−DMAC−water system. *Desalination* **1987**, *62*, 79−88.
(34) Yilmaz, L.; Mchugh, A. J. Analysis of nonsolvent−solvent−polymer phase diagrams and their relevance to membrane formation modeling. *J. Appl. Polym. Sci.* **1986**, *31*, 997−1018.
(35) Wang, D.; Li, K.; Teo, W. K. Porous PVDF asymmetric hollow fiber membranes prepared with the use of small molecular additives. *J. Membr. Sci.* **2000**, *178*, 13−23.
(36) Kimmerle, K.; Strathmann, H. Analysis of the Structure Determining Process of Phase Inversion Membranes. *Desalination* **1990**, *79*, 283−302.
(37) Wilke, C. R.; Chang, P. Correlation of diffusion coefficients in dilute solutions. *AIChE J.* **1995**, *12*, 264−270.
(38) Smolders, C. A.; Reuvers, A. J.; Boom, R. M.; Wienk, I. M. Microstructures in phase-inversion membranes. Part I. Formation of macrovoids. *J. Membr. Sci.* **1992**, *73*, 259−275.



https://dx.doi.org/10.1021/acsomega.0c05982
*ACS Omega* 2021, 6, 7444−7453